PHYSICAL REVIEW B **108**, 134419 (2023)

Evidence for a conical spin spiral state in the Mn triple layer on W(001): Spin-polarized scanning tunneling microscopy and first-principles calculations

Paula M. Weber,[1,*] Tim Drevelow,[2,†] Jing Qi,[1,‡] Matthias Bode,[1,3] and Stefan Heinze[2,4]
[1]*Physikalisches Institut, Experimentelle Physik II, Universität Würzburg, Am Hubland, 97074 Würzburg, Germany*
[2]*Institut für Theoretische Physik und Astrophysik, Christian-Albrechts-Universität zu Kiel, Kiel, Germany*
[3]*Wilhelm Conrad Röntgen-Center for Complex Material Systems (RCCM), Universität Würzburg, Am Hubland, 97074 Würzburg, Germany*
[4]*Kiel Nano, Surface, and Interface Science (KiNSIS), Christian-Albrechts-Universität zu Kiel, Kiel, Germany*

(Received 14 July 2023; accepted 27 September 2023; published 16 October 2023)

The spin structure of a Mn triple layer grown pseudomorphically on a W(001) surface is studied using spin-polarized scanning tunneling microscopy (SP-STM) and density functional theory (DFT). In SP-STM images a c(4×2) superstructure is found. The magnetic origin of this contrast is verified by contrast reversal and using the c(2×2) antiferromagnetic state of the Mn double layer as a reference. SP-STM simulations show that this contrast can be explained by a spin spiral propagating along the [110] direction with an angle close to 90° between magnetic moments of adjacent Mn rows. To understand the origin of this spin structure, DFT calculations have been performed for a large number of competing collinear and noncollinear magnetic states including the effect of spin-orbit coupling (SOC). Surprisingly, a collinear state in which the magnetic moments of the top Mn layer and the central Mn layer are aligned antiparallel and those of the bottom Mn layer are aligned parallel to those of the central layer is the energetically lowest state. We show that in this so-called "up-down-down" ($\uparrow\downarrow\downarrow$) state the magnetic moments in the Mn bottom layer are only induced by those of the central Mn layer. Flat spin spirals propagating in either one, two, or all Mn layers are shown to be energetically unfavorable to the collinear $\uparrow\downarrow\downarrow$ state even upon including the Dzyaloshinskii-Moriya interaction (DMI). However, conical spin spirals with a small opening angle of about 10° are only slightly energetically unfavorable within DFT and could explain the experimental observations. Surprisingly, the DFT energy dispersion of conical spin spirals including SOC cannot be explained if only the DMI is taken into account. Therefore higher-order interactions such as chiral biquadratic terms need to be considered, which could explain the stabilization of a conical spin spiral state.

DOI: 10.1103/PhysRevB.108.134419

I. INTRODUCTION

In ultrathin transition-metal films on surfaces, a great variety of intriguing magnetic states has been observed with atomic resolution using spin-polarized scanning tunneling microscopy (SP-STM), such as two-dimensional antiferromagnets [1–4], Néel states [5,6], flat and conical spin spiral states [7–9], multiple-Q states [10–12], chiral domain walls [13–15], or magnetic skyrmions [16–19]. The study of such structurally well-defined model systems allows complex spin structures to be understood on the basis of the underlying magnetic interactions. In this way, the interfacial Dzyaloshinskii-Moriya interaction (DMI) has been discovered [7,8], and higher-order exchange interactions have been revealed which can lead to three-dimensional spin structures [9–11,16].

So far, most of these studies have focused on systems consisting of one or two atomic layers of a magnetic material, such as Mn, Fe, or Co on a metallic surface. For spintronic devices, on the other hand, thicker film structures with at least a few atomic layers of a magnetic 3d transition metal are required which are interfaced with nonmagnetic metallic layers. Therefore it is interesting to extend studies at surfaces to systems with multiple magnetic layers. However, due to the lattice mismatch between the substrate and the magnetic film, such systems often exhibit complex structural relaxations and superstructures [20–23] that are hard to take into account in density functional theory (DFT) calculations. As a result, in such film systems an understanding of the spin structure and its origin from first-principles electronic structure theory is often limited.

In particular, for ultrathin Mn films on the (001) surface of body-centered cubic (bcc) tungsten (W) a large body of theoretical [24–27] and experimental research [4,8,28] is available. Even for the monolayer (ML) and the double layer (DL) these investigations revealed complex spin structures. In 2005, Dennler and Hafner proposed pseudomorphic growth of the Mn ML and DL on W(001) based on DFT calculations and predicted a ferromagnetic ground state due to hybridization with the substrate [25]. The ferromagnetic ground state of the Mn ML was found independently by Ferriani *et al.* at the same time via DFT calculations [24]. Indeed, low-energy electron diffraction (LEED) and Auger electron spectroscopy (AES) experiments confirmed the pseudomorphic growth of Mn on W(001) up to a film thickness of ≈16 Å, resulting in the body-centered tetragonal δ phase which adopts the lateral lattice constant of W(001), $a_W = 316.5$ pm [28].

---

[*] paula.weber@hhu.de
[†] drevelow@physik.uni-kiel.de
[‡] jing.qi@uni-wuerzburg.de

Intriguing magnetic properties, dependent on film thickness, have been experimentally reported for Mn/W(001). Ferriani *et al.* revealed that the Mn ML on W(001) exhibits a spin spiral state using SP-STM [8]. They explained this discrepancy compared with the predicted ferromagnetic state based on DFT as a result of the DMI [8] which occurs due to spin-orbit coupling not taken into account in the earlier DFT calculations [24,25]. For the Mn DL on W(001), a collinear antiferromagnetic (AFM) order with a magnetic c(2 × 2) unit cell and out-of-plane easy magnetization axis was observed [4], in contradiction to the predictions of Dennler and Hafner [25]. Interestingly, DFT calculations performed in the latter study revealed that the interfacial Mn layer is magnetically dead, i.e., it carries a vanishing magnetic moment, due to the strong hybridization with the W surface [4]. Theoretically, Dennler and Hafner predicted pseudomorphic growth and the transition from a ferromagnetic to an antiferromagnetic interlayer exchange coupling when going from the Mn DL to the Mn triple layer [25]. However, experimental results have not been available so far.

Here, we explore the structural and magnetic properties of a Mn triple layer (3L) on W(001) by combining SP-STM experiments with SP-STM simulations and DFT calculations. Experimentally, we find that 3L Mn indeed grows pseudomorphically on W(001). SP-STM reveals a $(2\sqrt{2} \times \sqrt{2})$ magnetic unit cell which can be consistently explained by a flat or a conical 90° spin spiral propagating along the [110] direction as shown by simulations of SP-STM images. Attempts to verify this spin structure as the magnetic ground state by DFT turned out to be highly intricate. Various spin structures, such as coplanar layered magnetic, antiferromagnetic, flat cycloidal, or conical spin spirals, and a superposition of two 90° spin spirals with opposite rotational sense (the so-called *uudd* state) are compared. In contrast to the work of Dennler and Hafner [25], we find that the energetically lowest collinear magnetic state exhibits an antiparallel alignment of the magnetic moments in the two upper Mn layers while the magnetic moments of the Mn interface layer are parallel to those of the central Mn layer.

Based on spin spiral calculations we show that the exchange interactions in the Mn triple layer are frustrated due to competing antiferromagnetic exchange couplings between and within the upper two Mn layers, an effect which is influenced by the Mn interlayer distances. In particular, we find that interlayer exchange prefers a collinear spin alignment while the intralayer exchange favors a spin spiral state. The DMI naturally promotes cycloidal spin spiral states. However, its energy contribution turns out to be rather small, which we attribute to the small induced magnetic moments of the Mn layer at the interface with the W substrate. The magnetocrystalline anisotropy as well as the magnetic dipole interaction are only about 0.05 meV/Mn atom and favor an in-plane magnetization. The 90° conical spin spiral states with a small opening angle—which can explain the SP-STM experiments—are still slightly higher in total energy than the collinear $\uparrow\downarrow\downarrow$ state. Surprisingly, we find that these DFT calculations can only be explained if we take higher-order interactions due to spin-orbit coupling into account such as the chiral biquadratic pair interaction.

II. EXPERIMENTAL METHODS

All experiments were performed in a two-chamber ultrahigh-vacuum (UHV) system with a base pressure $p \leqslant 1 \times 10^{-10}$ mbar. Clean W(001) was prepared in the preparation chamber by numerous cycles consisting of 5 min annealing at $T_{\text{ann}} = (1580 \pm 50)$ K in an oxygen atmosphere, followed by an ∼12-s-long high-temperature flash at $T_{\text{fl}} = (2400 \pm 100)$ K. To remove potential carbon from the surface and to avoid unwanted oxidation of W at the same time, we successively reduced the oxygen pressure from $p_{\text{O}_2} \simeq 5 \times 10^{-8}$ mbar in the initial cycle to $p_{\text{O}_2} \simeq 1 \times 10^{-9}$ mbar in the final cycle [29].

After the final cycle, the oxygen dosing valve was closed, and the W(001) crystal was flashed again for 15 s. Once the pressure dropped to $p < 3 \times 10^{-10}$ mbar, the Mn-loaded crucible of a commercial high-temperature effusion cell evaporator was preheated to a nominal temperature of 966.5 K for about 3 min to stabilize the evaporator and the pressure. Mn deposition onto the W(001) substrate was started at a sample temperature $T_{\text{s}} \approx 333$ K. During evaporation, the pressure indicated by the gauge was $p < 1 \times 10^{-9}$ mbar. After Mn deposition, the films were annealed at (493 ± 20) K for (14 ± 4) min. All Mn coverages mentioned below are given in pseudomorphic atomic layers (p-ALs) on W(001).

Immediately after preparation, the crystal was transferred into a home-built low-temperature STM housed in a UHV-compatible liquid He cryostat ($T_{\text{STM}} = 4.5$ K). We used electrochemically etched polycrystalline W tips. For spin-resolved STM measurements, these W tips were magnetized *in situ* by gently poking the tip apex into a Mn film (≈500 pm) and pulsing (≈10 V), similar to the description in Ref. [30]. All STM images were processed using WSXM [31].

III. COMPUTATIONAL DETAILS

We studied the structural, electronic, and magnetic properties of the Mn triple layer on W(001) using DFT. For structural relaxations of collinear magnetic states and to calculate the energy dispersion of spin spiral states, we used the full-potential linearized augmented plane-wave (FLAPW) method as implemented in the FLEUR code [32–34]. The relaxation of noncollinear magnetic states and all calculations in the c(4 × 2) supercell were carried out with the projector augmented wave (PAW) method as implemented in the Vienna *ab initio* simulation package (VASP) [35–37].

Structural relaxations with the FLEUR code were performed for collinear magnetic states in the generalized gradient approximation (GGA) using the exchange-correlation potential by Perdew and Wang [38]. We used the theoretical GGA lattice constant of W which amounts to $a = 3.17$ Å and differs from the experimental lattice constant by only 0.5%. Sixty-six k points were used in the irreducible part of the two-dimensional Brillouin zone. In these calculations for collinear magnetic states a symmetric film with a total of nine W layers and three Mn layers on either side was applied. The top three Mn and top two W layers were relaxed in the direction perpendicular to the film until the forces on each atom were below 0.001 hartrees/a.u. The muffin-tin spheres of the Mn and W atoms had radii of 2.3 and 2.5 a.u., respectively. The

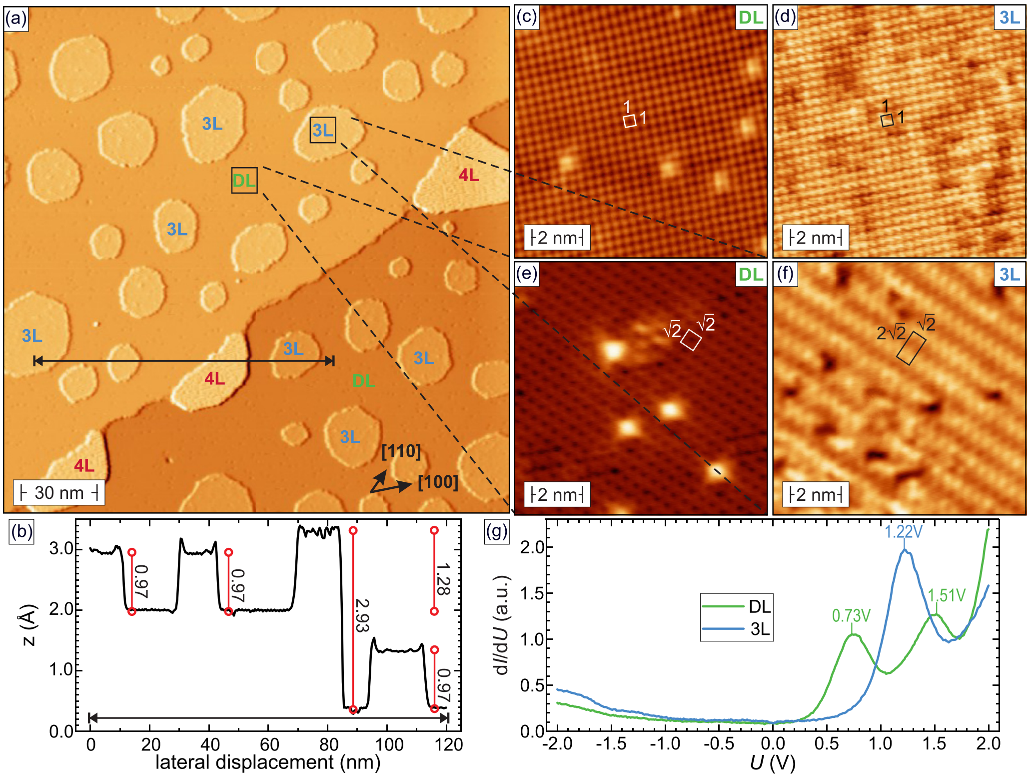

FIG. 1. (a) Overview STM topographic scan of a Mn film on W(001) with an average coverage $\theta_{\mathrm{Mn}}^{\mathrm{av}} = (2.3 \pm 0.2)$ p-ALs measured with a magnetic Mn/W tip. (b) Line profile measured between the points indicated by the double-headed black arrow in (a). (c) and (d) Spin-averaged atomic-resolution STM data taken on a DL Mn terrace (c) and a 3L Mn island (d). In both cases a square-shaped 1×1 unit cell is observed, indicating pseudomorphic growth. (e) and (f) Atomically spin-resolved SP-STM scans of DL and 3L Mn, respectively. A $\sqrt{2} \times \sqrt{2}$ magnetic unit cell is reproduced for DL in (e) (compare with Ref. [4]), whereas a $2\sqrt{2} \times \sqrt{2}$ structure is observed for 3L Mn in (f). (g) Tunneling spectra measured on DL Mn terraces (green) and 3L Mn islands (blue). Scan parameters are as follows: In (a), $U = 1$ V, $I = 300$ pA; in (c) and (f), $U = 10$ mV, $I = 4$ nA; and in (d) and (e), $U = 10$ mV, $I = 5$ nA. Stabilization parameters in (g) are $U = 2$ V, $I = 300$ pA.

plane-wave cutoff parameter was set to $k_{\max} = 4.0$ a.u.$^{-1}$, and the 5p semicore states of W were described by local p orbitals. The relaxation of the checkerboard antiferromagnetic state was done in a c(2×2) supercell on a 17×17 k-point grid with the $\uparrow\downarrow\uparrow$ state as a reference.

For spin spiral calculations in FLEUR, we used an asymmetric film consisting of nine W layers and a Mn triple layer on only one side of the film. The relaxed interlayer distances from the calculations for collinear magnetic states were used. The number of k points was increased to 2304 in the entire Brillouin zone, and the exchange-correlation potential was treated in the local density approximation (LDA) using the parametrization of Vosko, Wilk, and Nusair [39]. The plane-wave cutoff parameter $k_{\max} = 4.0$ a.u.$^{-1}$ and other settings remained unchanged from structural relaxation. The contribution of the DMI to the energy dispersion of spin spirals was obtained treating spin-orbit coupling (SOC) in first-order perturbation theory [40] since a self-consistent treatment of SOC is incompatible with the generalized Bloch theorem used for spin spirals. The calculation of the magnetocrystalline anisotropy energy was carried out in the same atomic setup including SOC self-consistently [41] and 18 225 k points in the total Brillouin zone with a plane-wave cutoff parameter $k_{\max} = 4.0$ a.u.$^{-1}$.

Structural relaxations in VASP were performed in a noncollinear setup to allow the relaxation of spin spiral states. A GGA exchange-correlation functional was used [42]. Calculations were carried out in the chemical unit cell using spin spiral boundary conditions, on a 22×22 k-point grid. An energy cutoff parameter of 300 eV was chosen for the plane-wave basis set. Atoms were arranged in the same symmetric slab with nine W layers as in the FLEUR calculations, where the top five layers are free to relax into the z direction, i.e., perpendicular to the surface. Collinear magnetic states were also relaxed to check consistency with the results obtained from FLEUR. For total energy calculations in the c(4×2) supercell the LDA exchange-correlation potential by Vosko, Wilk, and Nusair [39] was used together with an energy cutoff of 300 eV and a 12×24 grid of k points. The substrate was modeled asymmetrically by nine W layers with three Mn layers on one side. For calculations with SOC, the energy cutoff was increased to 390 eV, and the size of the k-point grid was increased to 18×36.

IV. RESULTS

A. Experimental results

The experimental results of our (SP-)STM experiments are summarized in Fig. 1. All data were taken on a W(001) sample which was coated with an average Mn coverage $\theta_{\mathrm{Mn}}^{\mathrm{av}} = (2.3 \pm 0.2)$ p-ALs. The 200×200-nm overview scan in Fig. 1(a) reveals smooth terraces which are covered by a Mn

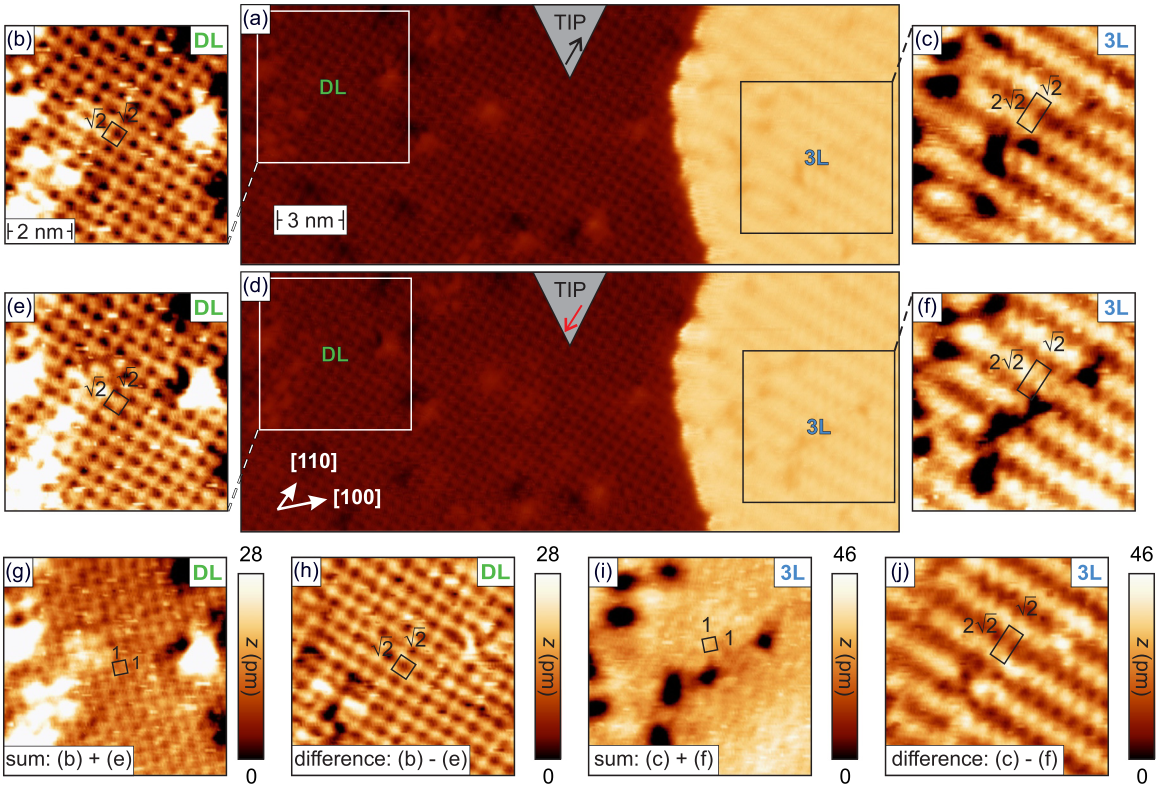

FIG. 2. (a) SP-STM image of a surface area covered by a double-layer (DL) and triple-layer (3L) Mn/W(001). (b) Zoomed image of the DL showing the well-known AFM $\sqrt{2} \times \sqrt{2}$ magnetic unit cell [4]. (c) Zoomed image of 3L Mn/W(001) with the $2\sqrt{2} \times \sqrt{2}$ magnetic unit cell. (d) SP-STM scan of the same area as shown in (a) but now measured with a reversed out-of-plane magnetic Mn/W tip. (e) and (f) Magnified views showing the magnetic structure of the Mn DL and 3L, respectively. (g) Sum and (h) difference of the images (b) and (e) taken on the Mn DL before and after tip magnetization reversal, respectively. Note that while (g) shows the structural unit cell and emphasizes the topographic signature of defects, (h) is dominated by the magnetic unit cell, and defects are almost invisible. (i) Sum and (j) difference of the images (c) and (f) taken on 3L Mn before and after tip magnetization reversal, respectively. Scan parameters in (a) and (d) are $U = 10$ mV, $I = 4$ nA.

double layer (DL) with numerous roughly circularly shaped Mn triple-layer (3L) islands on top. The typical island diameter is about 7 nm up to 30 nm. The line section plotted in Fig. 1(b) measured between the points indicated by the double-headed black arrow in Fig. 1(a) shows an apparent height of $h_{\mathrm{app}}^{3\mathrm{L}} \approx (100 \pm 20)$ pm at the tunneling parameters chosen here, i.e., a sample bias voltage $U = 1$ V and a tunneling current $I = 300$ pA. Moreover, semielliptical islands of the fourth Mn layer (4L) with diameters between 15 nm (perpendicular to the step edge) and 110 nm (along the step edge) and a height $h_{\mathrm{app}}^{4\mathrm{L}} \approx (290 \pm 20)$ pm can be found at step edges.

Atomic-resolution measurements performed with a nonmagnetic W tip on the flat terrace (covered by a Mn DL) and 3L Mn islands are presented in Figs. 1(c) and 1(d), respectively. As indicated by the white and black boxes, both data sets exhibit a square-shaped 1 × 1 unit cell with a lattice constant consistent with the underlying W(001) substrate, $a_{\mathrm{W}} = 316.5$ pm. Magnetically sensitive SP-STM data acquired on surface areas covered by Mn DL or 3L [indicated in Fig. 1(a)] are shown in Figs. 1(e) and 1(f), respectively. For the former, we recognize a $\sqrt{2} \times \sqrt{2}$ unit cell which is rotated by 45° with respect to the [100] direction of the W(001) substrate. The contrast is dominated by holes (depressions) surrounded by a grid of linear elevations. As discussed in detail in Ref. [4], this meshlike appearance in STM images is characteristic for the out-of-plane antiferromagnetic Mn DL on W(001).

Figure 1(f) presents typical atomic-resolution SP-STM data taken on a 3L Mn island. Zigzag-shaped stripes with an interstripe separation of (1.03 ± 0.14) nm and a periodicity of (0.49 ± 0.05) nm along the stripes are observable, corresponding to a $2\sqrt{2} \times \sqrt{2}$ magnetic unit cell indicated by a black rectangle. As shown in Fig. 1(g), by recording local tunneling spectra, we detect a very different local electronic structure for DL and 3L Mn. Whereas the DL exhibits peaks at $U = +0.73$ V and $U = +1.51$ V (green curve), the tunneling spectrum of 3L Mn yields only one characteristic peak at $U = +1.22$ V.

To unambiguously confirm the magnetic origin of the zigzag-shaped contrast observed in Fig. 1(f), we performed experiments in which the same locations covered by DL and 3L Mn on W(001) were imaged by SP-STM before and after reversing the tip magnetization; see Fig. 2. A high-resolution SP-STM scan of a surface area covered by a Mn DL in the darker left part and by a 3L Mn film on the brighter right part is shown in Fig. 2(a). On both surface areas a significant magnetic contrast is obtained, as highlighted in the zoomed-in images presented in Figs. 2(b) and 2(c), respectively. Since it is known from DFT calculations that the spin structure of the Mn DL on W(001) is out-of-plane antiferromagnetic [4], we can safely conclude that the tip magnetization must exhibit a significant out-of-plane component. Yet, the absolute magnetization direction of the tip is unknown, and the scheme in the upper part of Fig. 2(a) serves illustrative purposes only. We also note that we cannot exclude that this out-of-plane magnetization coexists with an in-plane component.

To reverse the out-of-plane component of the tip magnetization, the separation between the Mn/W tip and the sample was temporarily decreased by distance Δz. To exclude any effect on the previously imaged surface areas, the approach of the tip toward the Mn film was performed about 23 nm below the region shown in Fig. 2(a). At $\Delta z \approx 250$ pm, we suspect that tip and sample orbitals overlap at such close tip-sample distance, resulting in a significant exchange interaction [43–47] which magnetically reverses the Mn cluster at the tip apex.

Upon performing this procedure we moved back to the position of Fig. 2(a) and scanned the same surface area with a reversed tip magnetization; see Fig. 2(d). Zoomed-in scans of the Mn DL and 3L are shown in Figs. 2(e) and 2(f), respectively. Again the characteristic $\sqrt{2} \times \sqrt{2}$ and $2\sqrt{2} \times \sqrt{2}$ magnetic unit cells are observable. By using defect sites as markers to precisely align the images shown in Figs. 2(b) and 2(e) for the DL, a half-period shift of the magnetic contrast becomes evident. This first impression is corroborated by calculating the sum [Fig. 2(g)] and the difference [Fig. 2(h)] of the DL images displayed in Figs. 2(b) and 2(e). Whereas the sum in Fig. 2(g) exhibits the square-shaped 1×1 structural unit cell, the difference [Fig. 2(h)] demonstrates the familiar AFM $\sqrt{2} \times \sqrt{2}$ magnetic unit cell, in agreement with Ref. [4], thereby unambiguously confirming the reversal of the out-of-plane component of the tip magnetization.

Application of the same procedure to the SP-STM data presented in Figs. 2(c) and 2(f), which were obtained on the 3L region, results in the images presented in Fig. 2(i) for the sum and Fig. 2(j) for the difference. While the sum [Fig. 2(i)] yields a blurred signal only, possibly due to the very low structural atomic corrugation amplitude of 3L Mn on W(001), the difference image presented in Fig. 2(j) clearly reveals the magnetic $2\sqrt{2} \times \sqrt{2}$ unit cell, which can also be referred to as the magnetic c(4×2) unit cell. Please note that the defects are hardly visible in Fig. 2(j) but very pronounced in Fig. 2(i), indicating that the difference image tends to cancel topographic contrast and highlights magnetic contrast.

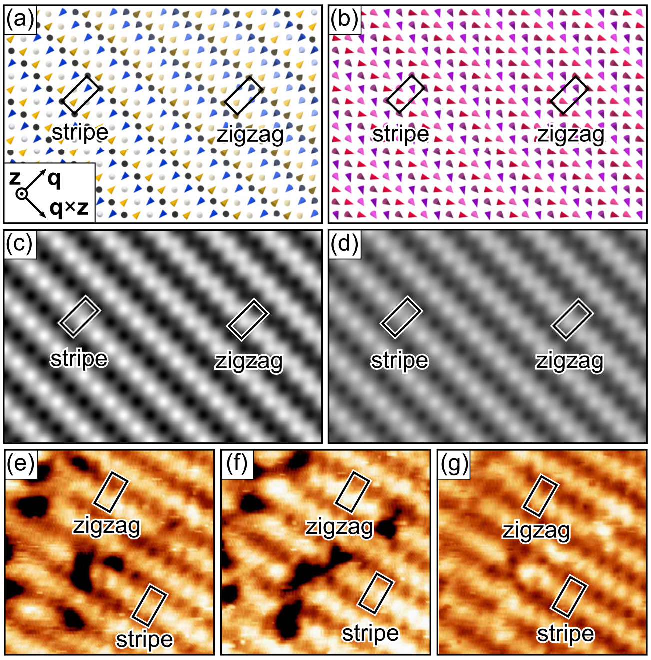

FIG. 3. Simulation of SP-STM images of a flat spin spiral [(a) and (c)] and a conical spin spiral [(b) and (d)], propagating into the direction **q** indicated and exhibiting an angle of 87.5° between the magnetic moments of Mn atoms in adjacent rows of the top layer. (a) and (b) show atomic magnetic moments in the top Mn layer. (c) and (d) show simulated magnetic contrast of SP-STM images according to the Tersoff-Hamann model for a magnetic tip with a magnetization direction perpendicular to the surface, i.e., in the z direction with normalized contrast. In both simulated images a zigzag domain and a stripe domain can be found, which are also observed in the SP-STM images displayed in (e) and (f) as well as in their difference in (g). Note that (e)–(g) are the same as Figs. 2(c), 2(f), and 2(j).

B. SP-STM simulations

The c(4×2) supercell suggested by the experimental SP-STM images as the magnetic unit cell of the Mn triple layer can be explained by a 90° spin spiral state propagating along the [110] direction of the surface. In such a state the magnetic moments of Mn atoms in adjacent rows perpendicular to the propagation direction are rotated by 90°, and the spiral completes a rotation after four lattice sites, which exactly matches the c(4×2) supercell. To check whether the experimentally observed contrast can be reproduced by assuming such a spin spiral state, we have simulated SP-STM images (Fig. 3) based on the spin-polarized generalization [48] of the Tersoff-Hamann model [49] using the model described in Ref. [50]. Note that in these SP-STM simulations only the magnetic moment directions of the Mn atoms in the surface layer enter, whereas the other two Mn layers have no impact on the simulated images.

For the SP-STM simulations we actually chose an angle of 87.5° between the magnetic moments of Mn atoms in adjacent rows of the top layer [Fig. 3(a)] instead of 90° as this leads to an even better matching of the experimental images. In particular, we observe the formation of different rotational domains (contrasts) on a larger scale while leaving the spin structure locally close to the 90° spiral. The two domains are denoted as stripe and zigzag domains [Figs. 3(a) and 3(c)]. In the stripe domain the Mn magnetic moments and the magnetization direction of the STM tip enclose angles of 0°, 90°, or 180°, while in the other domain a zigzag contrast is found due to enclosing angles of about 45° and 135° [Fig. 3(e)]. These two types of contrast also appear in the experimental images [Figs. 3(e)–3(g)].

However, a conical spin spiral with a finite opening angle and an angle of 87.5° between the flat spin spiral component of the magnetic moments of Mn atoms in adjacent rows [Figs. 3(b) and 3(d)] can explain the experimental observations as well. SP-STM simulations reveal that the magnetic

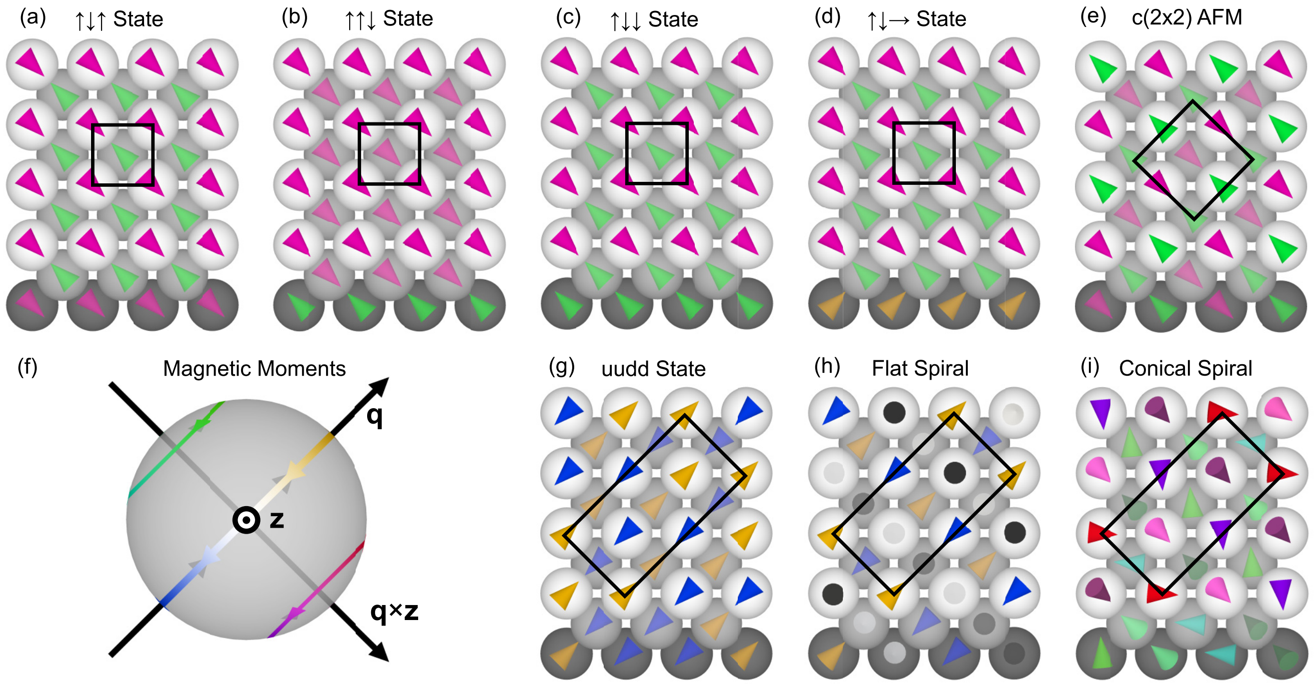

FIG. 4. Sketches of selected magnetic configurations investigated in the DFT study. The magnetic moments are indicated for Mn atoms in the top layer (white spheres), in the central layer (light gray spheres), and in the bottom layer (dark gray spheres). (a)–(e) Coplanar magnetic states with parallel magnetic moments in each layer. Note that the spin states in (a)–(d) do not lead to the observation of a magnetic superstructure in SP-STM images. The spin structures differ in the magnetic alignment of the bottom Mn layer. (f) Stereographic projection of the magnetic moments from the flat and conical spin spiral onto a sphere. Spin spirals lie at the intersection with a cone. The arrowheads show the sense of rotation of the moments when moving along **q**, as it is preferred by the Dzyaloshinskii-Moriya interaction. (g) *uudd* state that leads to a c(4×2) magnetic superstructure and is created by a superposition of two 90° spin spirals with opposite rotational sense. (h) Flat cycloidal spin spiral with an angle between adjacent moments within a Mn layer close to 90°. (i) Conical spin spiral with an opening angle of 40° which is a superposition of the states in (c) and (h).

contrast only changes in magnitude when going from a flat towards a conical spiral [Fig. 3(c) vs 3(d)]. The magnetic contrast of conical spirals cannot be distinguished from a flat spin spiral as long as the magnetization direction of the STM tip and the direction of the in-plane component are perpendicular to each other. This is consistent with the experimental situation since the easy magnetization direction of the ↑↓↓ state obtained in DFT is in the plane of the film (see Sec. IV C) and the STM tips had an out-of-plane magnetization direction as deduced from the contrast on the Mn double layer.

C. First-principles calculations

Structural relaxations and collinear states. First we performed DFT calculations for three collinear magnetic states to determine the exchange coupling between the upper and lower two Mn layers [Figs. 4(a)–4(c)]. The investigated states were the layerwise antiferromagnetic (↑↓↑) state [Fig. 4(a)] and two states in which the magnetic moments of two adjacent Mn layers are parallel and antiparallel with respect to the other Mn layer, i.e., the ↑↑↓ state [Fig. 4(b)] and the ↑↓↓ state [Fig. 4(c)], where each arrow denotes the magnetization of one Mn layer from top to bottom. Note that we could not converge the ferromagnetic (↑↑↑) state in our DFT calculations as the magnetic moments of the Mn layers flipped such that we arrived at the ↑↓↓ state.

We carried out structural relaxations for each of the collinear magnetic states using both the FLEUR code and the VASP code, which give similar results (Table I). Our results show that there is a large inward relaxation of the Mn layers which depends sensitively on the considered magnetic state. For the layerwise antiferromagnetic (↑↓↑) state, the relaxations and magnetic moments are in good agreement with those of a previous DFT study on the Mn triple layer on W(001) by Dennler and Hafner [25], as shown in Table I. Note that only the ferromagnetic state and the ↑↓↑ state were considered in that work [25].

Surprisingly, the ↑↓↓ state [Fig. 4(c)] is energetically much more favorable than the ↑↓↑ state in both the FLEUR and the VASP calculations (Table I). This indicates antiferromagnetic coupling between magnetic moments of the two upper Mn layers and ferromagnetic coupling between the Mn moments of the central and bottom layers. The magnetic moment of the interfacial (bottom) Mn layer is much smaller than that of the other two Mn layers. The magnetic moment of the bottom Mn layer vanishes if the moment direction is constrained within the FLEUR calculations to be perpendicular to the magnetic moments of the two upper layers [Fig. 4(d)]. This indicates that the Mn atoms at the W interface obtain

TABLE I. Results of structural relaxations of the Mn triple layer on W(001) for selected magnetic states (cf. Fig. 4) obtained via the FLEUR and VASP codes. In the table the c(2 × 2) AFM state has been abbreviated as "AFM", and the 90° spin spiral along $\overline{\Gamma' M}$ has been abbreviated as "$\overline{\Gamma' M}$". The relative changes d in percent of the interlayer distances with respect to the W bulk interlayer distance of 1.59 Å are given between the top (T), middle (M), and bottom (B) Mn layers as well as between the three top W layers. The difference in total energy ΔE relative to the ↑↓↑ state is given in meV/Mn atom. The magnetic moments of the Mn atoms are given in μ_B. For comparison the results of Dennler and Hafner [25] for the states considered in that work are given in the last two rows.

State	Method	$d_{T/M}$	$d_{M/B}$	$d_{B/1}$	$d_{1/2}$	$d_{2/3}$	ΔE	m_T	m_M	m_B
↑↓↑	FLEUR	−19.5	−5.5	−10.9	1.0	2.3	0	3.71	−3.04	2.36
↑↓↓	FLEUR	−32.8	−6.5	−16.1	4.3	1.0	−122	3.45	−2.92	−1.27
↑↑↓	FLEUR	−7.3	−23.9	−2.5	−1.6	3.2	35	3.75	2.37	−2.39
AFM	FLEUR	−17.7	−15.1	−13.0	2.9	−1.64	−36	±3.70	±2.87	∓0.90
↑↓↑	VASP	−24.4	−4.0	−15.8	0.5	−0.6	0	3.67	−3.13	1.90
↑↓↓	VASP	−31.9	−7.8	−16.4	2.1	−0.5	−145	3.28	−2.79	−1.40
↑↑↓	VASP	−8.3	−24.7	−3.8	−3.4	0.9	8	3.72	2.36	−2.39
$\overline{\Gamma' M}$	VASP	−27.2	−9.8	−15.7	1.6	−0.5	−90	−3.47	−2.90	−1.35
↑↓↑	Ref. [25]	−20.0	−5.4	−12.6	−0.6	−0.5	0	3.78	−3.14	2.39
↑↑↑	Ref. [25]	−13.1	−21.7	−14.5	0.7	−0.8	97	3.71	1.34	1.43

their magnetic moment in this state due to spin polarization by the two upper Mn layers.

We also observe a strong coupling of magnetic and geometric structure, with a tight binding for antiferromagnetic coupling between the two upper layers and a larger interlayer distance for a ferromagnetic alignment. Note that the strong inward relaxation of the top Mn layer in the ↑↓↓ state is consistent with the small apparent height difference between the Mn DL and 3L (cf. Fig. 1).

Our result for the Mn triple layer is consistent with a DFT study for the Mn double layer on W(001) which also indicated a preferred ferromagnetic coupling between adjacent layers [4]. Due to the c(2 × 2) antiferromagnetic state in the surface Mn layer of the double layer, the magnetic moment of the interfacial Mn layer is quenched in Mn-DL/W(001), indicating that it is also only induced by the adjacent Mn layer [4]. The antiferromagnetic coupling between magnetic moments of the upper Mn layers is also consistent with the DFT calculations of Dennler and Hafner [25]. The same type of coupling occurs in δ-Mn due to the weakened influence of the W substrate.

Spin spiral calculations. We have shown that the magnetic contrasts observed in the SP-STM images can be explained by a spin spiral state with an angle of about 87.5° (Fig. 3). Therefore we have performed DFT total energy calculations for spin spiral states. Spin spirals are spatially rotating magnetic structures characterized by a spiral vector $\mathbf{q}$ in reciprocal space [see Figs. 4(f) and 4(h)]. The magnetic moment $\mathbf{m}_i(\mathbf{q})$ at site i at the position $\mathbf{R}_i$ is given by

$$\mathbf{m}_i(\mathbf{q}) = m_{L(i)}[\cos(\mathbf{R}_i \cdot \mathbf{q}) \cdot \hat{\mathbf{z}} + \sin(\mathbf{R}_i \cdot \mathbf{q}) \cdot \hat{\mathbf{q}}], \qquad (1)$$

where $m_{L(i)}$ is the magnitude of the magnetic moment in layer $L(i) \in \{\mathrm{T}, \mathrm{M}, \mathrm{B}\}$ (see Table I). Equation (1) describes a cycloidal spin spiral that rotates in the zq plane.

High-symmetry points of the two-dimensional Brillouin zone [2D BZ, inset of Fig. 5(a)] correspond to collinear magnetic states. At the $\overline{\Gamma}$ point we find the ↑↑↓ state [Fig. 4(b)], at the $\overline{\Gamma}'$ point we find the ↑↓↓ state [Fig. 4(c)], at the $\overline{M}$ point we find the c(2 × 2) AFM state [Fig. 4(e)], and at the $\overline{X}$ point we find the p(2 × 1) AFM state. For a spin spiral vector $\mathbf{q}$ halfway along the high-symmetry direction $\overline{\Gamma' M}$, one obtains a spin spiral with angles of 90° between adjacent Mn moments within a layer [Fig. 4(h)], which could explain the SP-STM measurements. Note that the orientation of the plane in which the spins rotate is not fixed as long as spin-orbit coupling is neglected.

Starting from the energetically preferred ↑↓↓ state at the $\overline{\Gamma'}$ point of the 2D BZ, $\mathbf{q}$ was varied for a spiral propagating in all Mn layers, which results in the energy dispersion $E(\mathbf{q})$ shown in Fig. 5(a). In order to check the influence of the structure of the Mn triple layer, spin spiral calculations were performed for four different geometries corresponding to the relaxed structure of the ↑↓↓ state, the 90° spin spiral along $\overline{\Gamma' M}$, a c(2 × 2) antiferromagnetic state in all magnetic layers, and the ↑↓↑ state (cf. Table I). Interlayer distances for all geometries were taken from the FLEUR calculations, except for the 90° spin spiral geometry, which was taken from the VASP calculations.

The energy minimum of $E(\mathbf{q})$ lies for all geometries at the $\overline{\Gamma'}$ point, i.e., at the ↑↓↓ state [Fig. 5(a)]. The spin spiral energy increases as $\mathbf{q}$ is varied along the $\overline{\Gamma' X}$ and $\overline{\Gamma' M}$ directions of the two-dimensional Brillouin zone and reaches its maximum at the $\overline{\Gamma}$ point of the first Brillouin zone, i.e., at the ↑↑↓ state. However, the curvature of $E(\mathbf{q})$ in the vicinity of $\overline{\Gamma'}$ depends significantly on the structural relaxation, i.e., the Mn interlayer distances. The 90° flat spin spiral at $\overline{\Gamma' M}/2$ which can explain the SP-STM images (Fig. 3) is not favored in our DFT calculations neglecting spin-orbit coupling over the ↑↓↓ state in any of the investigated geometries. In its own ground state geometry its energy is 25 meV/Mn atom higher than the ↑↓↓ state [Fig. 5(a)]. For the structure of the c(2 × 2) AFM state, the energy of the 90° spin spiral state is only 10 meV/Mn atom above the energy of the ↑↓↓ state.

The magnetic moments in each Mn layer [Fig. 5(b)] display only a small variation for spin spiral states in the vicinity of the energy minimum at the $\overline{\Gamma'}$ point (↑↓↓ state). However, as the spin spiral vector $\mathbf{q}$ approaches the $\overline{X}$ and $\overline{\Gamma}$ points, the magnetic moments of the central and bottom Mn layers vary significantly. Especially the moment of the interfacial Mn

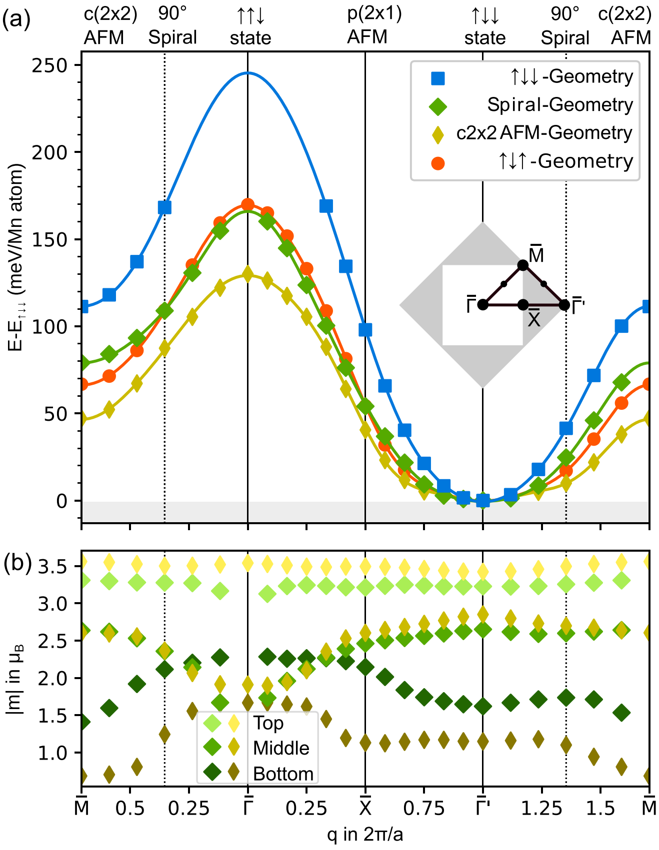

FIG. 5. (a) Energy dispersion $E(\mathbf{q})$ of spin spirals propagating in the Mn triple layer on W(001). Data points represent DFT total energies obtained without SOC, while connecting curves are a fit to the atomistic spin model. Calculations were carried out for the relaxed geometries (cf. Table I) of four different magnetic states: the ↑↓↓ state (blue squares), the 90° spin spiral state along $\overline{\Gamma' M}$ (green diamonds), the c(2 × 2) AFM state (yellow diamonds), and the ↑↓↑ [layered antiferromagnet (LAFM)] state (orange circles). The spin spiral vectors $\mathbf{q}$ are chosen along the high-symmetry directions of the first (white square) and second (gray diamond) Brillouin zones (see inset). (b) Magnetic moments for each Mn layer of a spin spiral with the ground state geometry of the 90° spin spiral along $\overline{\Gamma' M}$ (shades of green) and the c(2 × 2) antiferromagnet (shades of yellow).

layer changes over a range from 0.7 to 1.7 μ_B, presumably because its magnetism is induced from the upper layers.

The energy dispersion $E(\mathbf{q})$ calculated via DFT for spin spirals neglecting spin-orbit coupling [Fig. 5(a)] can be used to parametrize an effective atomistic spin model including only Heisenberg exchange interactions. For simplicity, the triple layer is modeled as a single magnetic layer with one type of magnetic atoms. The spins in the model are placed in a plane at the xy coordinates of the Mn atoms in the trilayer. Thereby, the top- and bottom-layer Mn atoms are mapped to a single site, while the middle layer represents another site of the effective square spin model with a nearest-neighbor distance of $a/\sqrt{2}$. Since there is only one species of atoms in the effective spin model, interactions of atoms that have the same distance within the xy plane, i.e., Mn atoms from the top and bottom layers, will be added together. The predictions of the effective model for each energy dispersion are displayed as the solid curves in Fig. 5(a). The parameters of the effective model are listed in Table II.

The exchange interaction between nearest neighbors is the dominating interaction in the spin model of the film ranging from a maximum antiferromagnetic strength of $J_1^{\text{eff}} = -7.85$ meV for the ↑↓↓ ground state geometry to a minimal strength of $J_1^{\text{eff}} = -4.39$ meV for the c(2 × 2) AFM ground state geometry. This interaction is the sum of the interactions between nearest neighbors in the top and middle layers and the interactions between nearest neighbors in the middle and bottom layers in the trilayer, making it an interlayer interaction. This result is consistent with the above investigation of interlayer coupling based on collinear magnetic states (cf. Table I), in which the antiferromagnetic coupling between the top and middle layers dominates the ferromagnetic coupling between the bottom two layers. The most preferable magnetic state for a negative J_1^{eff} is a c(2 × 2) antiferromagnetic state in the effective spin model, which translates to a triple layer with ferromagnetically aligned layers that have an antiferromagnetic coupling between the layers consistent with the ↑↓↓ state. The next-nearest exchange interaction, J_2^{eff}, also prefers an antiferromagnetic coupling ($J_2^{\text{eff}} < 0$). It represents the nearest-neighbor intralayer interaction, and the next-nearest-neighbor interaction between the top and bottom Mn layers. J_2^{eff} competes with J_1^{eff}, since the ferromagnetic state in each layer that is stabilized by J_1^{eff} is energetically the least optimal state for a negative J_2^{eff}. For a larger ratio $J_2^{\text{eff}}/J_1^{\text{eff}}$, a spin spiral ground state is expected for the atomistic spin model. The same holds for J_3^{eff}, which is similar to J_2^{eff} in sign and strength. Exchange constants beyond J_3^{eff} are quite small in comparison to J_1^{eff} and have negligible influence of the magnetic ground state of the spin model, leading to a checkerboard antiferromagnetic pattern that represents the ↑↓↓ in the real system. For the c(2 × 2) AFM ground state geometry, the competing contributions of interlayer and intralayer exchange to the energy dispersion $E(\mathbf{q})$ can be seen in Fig. 6(a). In Fig. 6(a) it is apparent that the two types of exchange interactions compete as the intralayer exchange prefers a spin spiral state while the interlayer exchange favors the collinear ↑↓↓ state.

The 90° spin spiral can be used to create another state that is also consistent with the c(4 × 2) magnetic unit cell suggested by the SP-STM measurements: a superposition of two 90° spin spirals with opposite rotational sense leading to the *uudd* state [51] [see Fig. 4(g)]. This state has recently been observed in hexagonal magnetic monolayers on surfaces [10,52]. On a bcc (001) surface, it exhibits a c(4 × 2) magnetic unit cell. It is degenerate in energy with the 90° spin spiral within the Heisenberg model of pairwise exchange. Total energy differences obtained by DFT calculations must stem from higher-order interactions [10,51,53]. We calculated the total energies of an *uudd* state and a 90° spin spiral with the VASP code in a c(4 × 2) supercell using the relaxed geometry of the ↑↓↓ state. The obtained energies of 37 meV/Mn atom for the 90° spiral with respect to the ↑↓↓ state, which is consistent with the FLEUR result, and 60 meV/Mn atom for the *uudd* state with respect to the ↑↓↓ state show that higher-order interactions favor the 90° spin spiral over the *uudd* state. Note that the *uudd* state differs from the 87.5° spin spiral state in that its SP-STM image only shows a zigzag

TABLE II. Effective exchange constants, J_i^{eff}, for ith neighbors obtained by fitting the energy dispersions of the 3L Mn/W(001) [Fig. 5(a)] for different ground state geometries to an effective single magnetic layer spin model. In the table the c(2 × 2) AFM state has been abbreviated as "AFM", and the 90° spin spiral along $\overline{\Gamma' M}$ has been abbreviated as "$\overline{\Gamma' M}$". The exchange constants are given in meV.

Geometry	J_1^{eff}	J_2^{eff}	J_3^{eff}	J_4^{eff}	J_5^{eff}	J_6^{eff}	J_7^{eff}	J_8^{eff}	J_9^{eff}
↑↓↓	−7.85	−0.40	−0.58	0.09	−0.09	0.04	0.03	−0.03	0.02
↑↓↑	−5.50	−0.65	−0.65	0.17	−0.07	−0.02	0.04	−0.06	0.02
$\overline{\Gamma' M}$	−5.13	−0.05	−0.81	0.05	−0.05	−0.14	−0.04	−0.01	−0.01
AFM	−4.39	−0.66	−0.44	0.26	−0.01	−0.03	0.05	−0.08	0.02

pattern and cannot explain the observed stripe contrast (cf. Fig. 3).

Dzyaloshinskii-Moriya interaction. Since the DMI is known to favor spin spirals over the ferromagnetic state, we investigated whether the inclusion of SOC could lead to a noncollinear ground state in the Mn trilayer. The contributions of SOC to the total energies of spin spirals were calculated using FLEUR within first-order perturbation theory, starting from self-consistent cycloidal spin spiral states in the c(2 × 2) AFM ground state geometry [see Fig. 6(b)]. Negative energy values decrease the energy of counterclockwise rotating spirals, and positive values decrease the energy of clockwise rotating ones.

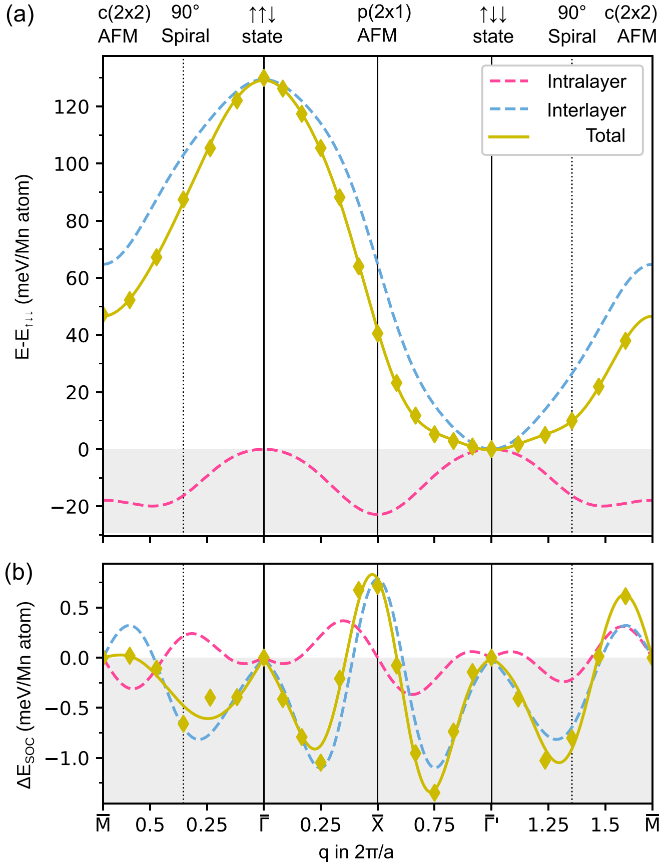

FIG. 6. Energy dispersion $E(\mathbf{q})$ of flat cycloidal spin spirals in the 3L Mn/W(001) for the ground state geometry of the c(2 × 2) AFM state. (a) Spin spiral energy without spin-orbit coupling (SOC). DFT total energies (yellow diamonds) are fitted with a model of bilinear exchange (yellow curve). Contributions of effective intralayer and interlayer exchange in the model are displayed in pink and blue, respectively. (b) SOC contribution to the energy dispersion of a cycloidal, counterclockwise rotating spin spiral, in first-order perturbation theory. The DFT data are fitted with the DMI of the effective spin model, which can also be separated into intralayer and interlayer contributions. Positive energy values imply the preference of a clockwise spiral by the same amount. Note that the interlayer interactions between the top Mn layer and the bottom Mn layer are mapped onto effective intralayer interaction in (a) and (b).

Energy contributions at the $\overline{X}$ point indicate the presence of interlayer DMI, since each layer exhibits a row-wise antiferromagnetic state at this high-symmetry point, i.e., a collinear state without intralayer DMI contributions. By mapping the energies to an effective monolayer system, as for the exchange interaction, it can be revealed that the interlayer DMI is the dominating term. Both interlayer DMI and intralayer DMI favor spin spiral states with an energy minimum along the $\overline{\Gamma' X}$ direction. Along the $\overline{\Gamma' M}$ direction the energy minimum is close to the 90° spin spiral. However, SOC contributions are two orders of magnitude smaller than the total energy of flat spin spirals without SOC.

Magnetic anisotropy. We obtained only a very small magnetocrystalline anisotropy energy of 0.01 meV/Mn atom for the ↑↓↓ state of the Mn triple layer on W(001) favoring an in-plane orientation of the magnetization. We attribute the small SOC effect to the fact that the bottom Mn layer at the interface to the W substrate exhibits only a small magnetic moment which is induced by the adjacent central Mn layer. Therefore the Mn layers with significant intrinsic magnetic moments are at a relatively large distance from the heavy W substrate needed to create large SOC effects.

To compute the influence of the magnetic dipole-dipole interactions, we numerically summed over the magnetic fields of atomic magnetic moments with a distance of up to 1000 in-plane lattice constants taking the geometrical structure and the magnetic moments of the three different Mn layers obtained from DFT for the ↑↓↓ state into account. From these calculations we found that the magnetostatic dipolar interaction favors an in-plane orientation of the magnetic moments in the ↑↓↓ state by 0.036 meV/Mn atom with respect to an out-of-plane orientation. This small value can be understood from the net magnetic moment of the Mn triple layer which amounts to only about 0.75 μ_B per unit cell (cf. Table I). The inclusion of SOC does not change the ground state of the system. DMI alone would prefer a spin spiral with a period of about 200 lattice constants by 4 μeV close to the ↑↓↓ state. However, the magnetocrystalline anisotropy raises the energy of all cycloidal spin spiral states by 6 μeV, thus stabilizing the collinear ground state.

Conical spin spiral states. We can obtain spin spiral states of lower energy than the flat 90° spin spiral by superimposing it with the ↑↓↓ state at each lattice site i, thereby constructing a conical spin spiral state with magnetic moments

$$\mathbf{m}_i(\mathbf{q},\theta) = \sin(\theta)\cdot\mathbf{m}_i(\mathbf{q}) + \cos(\theta)\cdot m_{L(i)}(\hat{\mathbf{q}}\times\hat{\mathbf{z}}), \qquad (2)$$

which is characterized by the opening angle θ that its moments and the rotational axis $\hat{\mathbf{q}}\times\hat{\mathbf{z}}$ enclose [Figs. 4(f) and 4(i)]. The total energy of a conical spin spiral can be described within the extended Heisenberg model by

$$E = -\sum_{ij} J_{ij}(\mathbf{m}_i\cdot\mathbf{m}_j) - \sum_{ij} B_{ij}(\mathbf{m}_i\cdot\mathbf{m}_j)^2, \qquad (3)$$

in which a biquadratic exchange term has been included as a higher-order interaction in the bilinear exchange. By computing the energy of the conical spin spiral from Eq. (2), the energy

$$E_{\mathbf{q}}(\theta) - E_{\uparrow\downarrow\downarrow} = J^{\mathrm{eff}}_{\mathbf{q}}\sin^2(\theta) + B^{\mathrm{eff}}_{\mathbf{q}}\sin^4(\theta) \qquad (4)$$

of a spiral with the vector $\mathbf{q}$ as a function of the opening angle can be derived. For small θ the energy comes close to the energy $E_{\uparrow\downarrow\downarrow}$ of the ↑↓↓ state. The first and second terms arise from bilinear and biquadratic exchange, respectively. The addition of higher-order exchange interactions such as the biquadratic term can lead to an energy minimum for a conical spin spiral as reported for a Mn DL on W(110) [9].

For the 90° spin spiral near the $\overline{\Gamma'}$ point, $E_{\mathbf{q}}(\theta)$ was calculated via DFT for three different ground state geometries [Fig. 7(a)]. The obtained total DFT energies closely follow a $\sin^2(\theta)$ dependence, indicating large contributions from bilinear exchange, i.e., the first term on the right-hand side of Eq. (4). Higher-order exchange contributions significantly improve the fit of the DFT data [Fig. 7(a)]. However, they are comparatively small and tend to favor flat spin spirals.

To investigate the influence of SOC, we have calculated the energy contribution due to SOC to the energy of conical spin spirals in the same computational setup using first-order perturbation theory via the FLEUR code. To model the effect of SOC on the energy within the atomistic spin model, we used

$$\Delta E_{\mathrm{SOC}} = -\sum_{ij}\mathbf{D}_{ij}(\mathbf{m}_i\times\mathbf{m}_j) - \sum_{ij}\mathbf{C}_{ij}(\mathbf{m}_i\times\mathbf{m}_j)\cdot(\mathbf{m}_i\cdot\mathbf{m}_j), \qquad (5)$$

which contains the DMI as well as the chiral biquadratic pair interaction that was recently proposed in Ref. [54]. The two vectors $\mathbf{D}_{ij}$ and $\mathbf{C}_{ij}$ are assumed to align perpendicular to the plane of rotation of the spiral. For the conical spin spiral, Eq. (2), the SOC energy

$$\Delta E_{\mathrm{SOC},\mathbf{q}}(\theta) = D^{\mathrm{eff}}_{\mathbf{q}}\sin^2(\theta) + C^{\mathrm{eff}}_{\mathbf{q}}\sin^4(\theta) \qquad (6)$$

has the same dependence on θ as the exchange energy. The second term arises because of the chiral biquadratic pair interaction.

The energy contribution $\Delta E_{\mathrm{SOC},\mathbf{q}}(\theta)$ calculated via DFT [Fig. 7(b)] depends strongly on the geometry of the film system, i.e., the Mn interlayer distances. For the c(2 × 2) AFM ground state geometry, the highest SOC contribution is computed for the flat spin spiral ($\theta = 90°$) with about 0.8 meV/Mn atom, preferring a counterclockwise rotation. The fit of the DFT data to Eq. (6) shows that the chiral biquadratic term plays a non-negligible role [Fig. 7(b)]. For the other two considered ground state geometries, the SOC energy for the flat spin spiral ($\theta = 90°$) decreases drastically to only 0.1 meV/Mn atom. However, for an opening angle θ of about 40°–50° we observe a change of the preferred rotational sense which cannot be explained by the DMI. This unexpected dependence of the SOC energy for conical spin spirals as a function of the opening angle stems from higher-

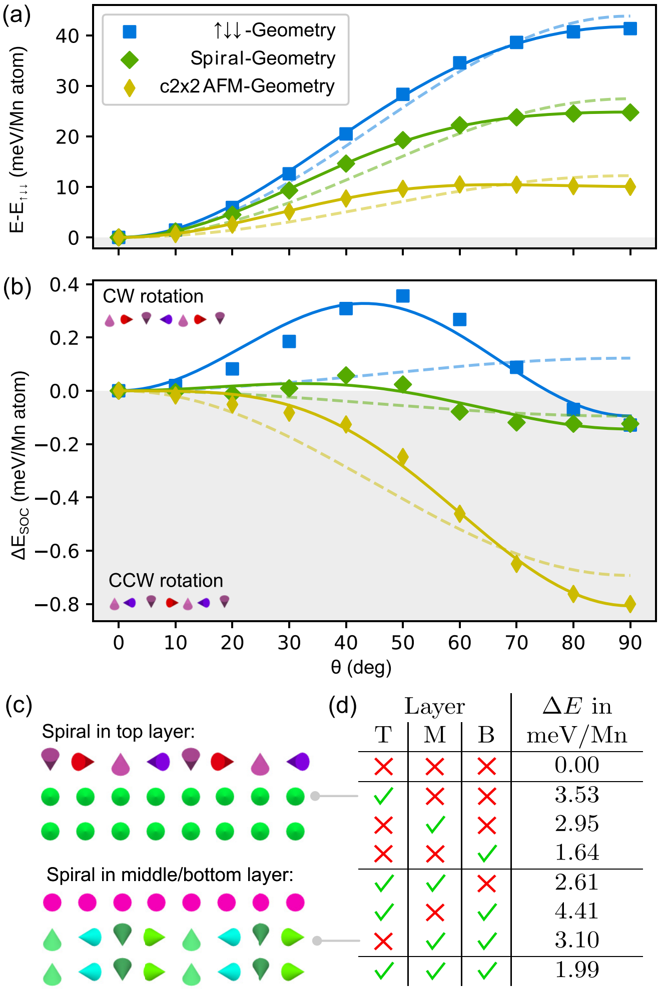

Layer			ΔE in
T	M	B	meV/Mn
✗	✗	✗	0.00
✓	✗	✗	3.53
✗	✓	✗	2.95
✗	✗	✓	1.64
✓	✓	✗	2.61
✓	✗	✓	4.41
✗	✓	✓	3.10
✓	✓	✓	1.99

FIG. 7. (a) Total DFT energies of conical 90° spin spirals in the 3L Mn/W(001) along the $\overline{\Gamma' M}$ direction as a function of the opening angle θ neglecting SOC. The dashed curves represent fits with only Heisenberg exchange, while the solid curves include also the biquadratic exchange [see Eq. (4)]. All calculations were performed in three different ground state geometries as indicated. (b) SOC contributions to the energy of conical spin spirals obtained via DFT in first-order perturbation theory. The dashed curves represent fits with only DMI, i.e., the first term of Eq. (6), while the solid curves include also the chiral biquadratic pair interaction, i.e., both terms of Eq. (6). CW, clockwise; CCW, counterclockwise. (c) Sketch of conical spin spirals in selected Mn layers. Ferromagnetic layers point towards the viewer, while spiral parts rotate in a perpendicular direction. (d) Total DFT energies without SOC of conical spin spirals propagating only in selected Mn layers, with an opening angle of $\theta = 10°$. The first three columns of the table indicate in which of the layers the spirals propagate (top, middle, and bottom layers).

order interactions due to SOC such as the chiral biquadratic term. Especially, for the ↑↓↓ ground state geometry there is a significant energy gain of about 0.4 meV/Mn atom for a clockwise rotating conical spin spiral with an opening angle of 50°. Nevertheless, the SOC contributions are at least one order of magnitude smaller, even in the c(2 × 2) AFM ground state geometry. Therefore, within our DFT calculations, SOC does not lead to a 90° conical spin spiral that would explain the experimental results.

We have also investigated whether the energy of the conical 90° spin spiral with an opening angle of $\theta = 10^\circ$ can be lowered by propagating it only in one or two of the Mn layers, while the other layers are in a ferromagnetic state [sketch in Fig. 7(c)]. The results of these calculations are collected in Fig. 7(d). All total energies are given with respect to the ↑↓↓ state and have been obtained neglecting SOC. While the creation of a spin spiral in one magnetic layer requires energy, less energy is needed for the creation of a second spiral. If both spin spirals propagate in the two top layers, it even lowers the energy with respect to the case of only one spin spiral. This can be explained by the strong antiferromagnetic coupling between the top two layers. The state with spin spirals in all three Mn layers possesses the lowest energy per spin spiral. Such a conical 90° spin spiral with an opening angle of $\theta = 10^\circ$ has an energy only about 2 meV/Mn atom higher than the energy of the ↑↓↓ state. The average energy needed for the creation of a spiral in each layer lies below 0.66 meV/Mn atom, which is even lower than the 1.64 meV/Mn atom for a spiral in the bottom layer. Note that the energy differences of conical spin spirals with respect to the ↑↓↓ state are expected to be even lower if the calculations are performed for a different structural relaxation similar to the result obtained for flat spin spirals [cf. Fig. 7(a)].

V. CONCLUSION

In our SP-STM experiments, we found the well-known meshlike $\sqrt{2} \times \sqrt{2}$ structure on the Mn DL on W(001), which was first described in Ref. [4]. This result is in perfect agreement with the c(2 × 2) AFM order in the surface Mn layer and quenched magnetic Mn moments at the Mn/W interface reported by Meyer *et al.* [4]. Our SP-STM data of pseudomorphic 3L Mn/W(001) films show periodic zigzag-patterned stripes consistent with a magnetic $2\sqrt{2} \times \sqrt{2}$ unit cell. The magnetic origin of this pattern was verified by experiments, where the tip magnetization was reversed at close tip-sample distance via the exchange interaction, resulting in a characteristic contrast inversion for both DL and 3L Mn; see Fig. 2. A limitation of these spin-polarized measurements lies in the uncertainty of the magnetization direction of the spin-polarized Mn/W tip, namely whether it is entirely out-of-plane magnetized or also includes a significant in-plane component.

SP-STM simulations revealed that a spin spiral state with an angle close to 90° can explain the observed magnetic contrast. A flat spin spiral as well as a conical spin spiral with a finite opening angle is consistent with the SP-STM experiments since the magnetization direction of the tip could not be fully determined.

DFT calculations have been performed using the FLEUR code as well as the VASP code to shed light on the magnetic ground state and its origin. Our calculations show that the geometric structure of the Mn triple layer and its magnetic state are closely linked. In particular, the interlayer distances between the Mn layers and between the bottom Mn layer and the W substrate change considerably upon changing the magnetic state in the triple layer.

We found a collinear magnetic state for the Mn triple layer on W(001) which is energetically much more favorable in DFT than the layered antiferromagnetic state previously proposed by Dennler and Hafner [25]. In this so-called ↑↓↓ state the magnetic moments of the Mn surface and central layers are oppositely aligned with respect to each other. The magnetic moments of the Mn atoms in the interface layer to the W substrate are aligned parallel to those of the central layer and only induced by the central Mn layer.

Spin spiral calculations performed starting from the ↑↓↓ state show a total DFT energy rise upon canting the spins, i.e., deviating from the collinear state. Therefore a flat 90° spin spiral state is unfavorable with respect to the ↑↓↓ state. However, the energy difference depends significantly on the interlayer distances in the Mn triple layer. We find that the interlayer exchange prefers the collinear state, while intralayer exchange interactions favor a spin spiral state. The DMI prefers a 90° cycloidal spin spiral state; however, its energy contribution is much smaller than that of the exchange. The magnetocrystalline anisotropy energy is also small in the ↑↓↓ state and favors an in-plane magnetization. We attribute the small size of the SOC effects to the small Mn moments at the W interface in the ↑↓↓ state.

DFT calculations for conical spin spiral states show that the energy still rises upon deviating from the collinear ↑↓↓ state; however, the energy difference is much reduced. Based on these results, we can exclude a significant effect of higher-order exchange interactions in the Mn triple layer which could be responsible for a conical spin spiral as found for a Mn DL on W(110) [9]. Surprisingly, we found that the energy contribution due to SOC for conical spin spirals deviates qualitatively from that expected by the DMI. Therefore higher-order interactions due to SOC such as the chiral biquadratic pair interaction need to be taken into account. Such interactions might explain the occurrence of a conical spin spiral state in the Mn triple layer since the 90° conical spin spiral state with a small opening angle of 10°—which can explain the observed SP-STM images—is only slightly higher in energy than the ↑↓↓ state. Different opening angles of the conical spin spiral state in the three Mn layers not considered in our DFT calculations might also further lower its total energy.

ACKNOWLEDGMENTS

We would like to thank S. Meyer for fruitful discussions and S. Haldar for technical support with the VASP calculations. We acknowledge support by DFG through Würzburg-Dresden Cluster of Excellence (ct.qmat). T.D. and S.H. gratefully acknowledge financial support from the Deutsche Forschungsgemeinschaft (DFG, German Research Foundation) via Project No. 418425860 and the SPP2137 “Skyrmionics” project (Project No. 462602351) and computing time provided by the North-German Supercomputing Alliance (HLRN).

[1] S. Blügel, M. Weinert, and P. H. Dederichs, Ferromagnetism and antiferromagnetism of 3d-metal overlayers on metals, Phys. Rev. Lett. **60**, 1077 (1988).

[2] S. Heinze, M. Bode, A. Kubetzka, O. Pietzsch, X. Nie, S. Blügel, and R. Wiesendanger, Real-space imaging of two-dimensional antiferromagnetism on the atomic scale, Science **288**, 1805 (2000).

[3] A. Kubetzka, P. Ferriani, M. Bode, S. Heinze, G. Bihlmayer, K. von Bergmann, O. Pietzsch, S. Blügel, and R. Wiesendanger, Revealing antiferromagnetic order of the Fe monolayer on W(001): Spin-polarized scanning tunneling microscopy and first-principles calculations, Phys. Rev. Lett. **94**, 087204 (2005).

[4] S. Meyer, M. Schmitt, M. Vogt, M. Bode, and S. Heinze, Dead magnetic layers at the interface: Moment quenching through hybridization and frustration, Phys. Rev. Res. **2**, 012075(R) (2020).

[5] C. L. Gao, W. Wulfhekel, and J. Kirschner, Revealing the 120° antiferromagnetic Néel structure in real space: One monolayer Mn on Ag(111), Phys. Rev. Lett. **101**, 267205 (2008).

[6] M. Waśniowska, S. Schröder, P. Ferriani, and S. Heinze, Real space observation of spin frustration in Cr on a triangular lattice, Phys. Rev. B **82**, 012402 (2010).

[7] M. Bode, M. Heide, K. von Bergmann, P. Ferriani, S. Heinze, G. Bihlmayer, A. Kubetzka, O. Pietzsch, S. Blügel, and R. Wiesendanger, Chiral magnetic order at surfaces driven by inversion asymmetry, Nature (London) **447**, 190 (2007).

[8] P. Ferriani, K. von Bergmann, E. Y. Vedmedenko, S. Heinze, M. Bode, M. Heide, G. Bihlmayer, S. Blügel, and R. Wiesendanger, Atomic-scale spin spiral with a unique rotational sense: Mn monolayer on W(001), Phys. Rev. Lett. **101**, 027201 (2008).

[9] Y. Yoshida, S. Schröder, P. Ferriani, D. Serrate, A. Kubetzka, K. von Bergmann, S. Heinze, and R. Wiesendanger, Conical spin-spiral state in an ultrathin film driven by higher-order spin interactions, Phys. Rev. Lett. **108**, 087205 (2012).

[10] A. Krönlein, M. Schmitt, M. Hoffmann, J. Kemmer, N. Seubert, M. Vogt, J. Küspert, M. Böhme, B. Alonazi, J. Kügel, H. A. Albrithen, M. Bode, G. Bihlmayer, and S. Blügel, Magnetic ground state stabilized by three-site interactions: Fe/Rh(111), Phys. Rev. Lett. **120**, 207202 (2018).

[11] J. Spethmann, S. Meyer, K. von Bergmann, R. Wiesendanger, S. Heinze, and A. Kubetzka, Discovery of magnetic single- and triple-**q** states in Mn/Re(0001), Phys. Rev. Lett. **124**, 227203 (2020).

[12] M. Gutzeit, A. Kubetzka, S. Haldar, H. Pralow, M. Goerzen, R. Wiesendanger, S. Heinze, and K. von Bergmann, Nano-scale collinear multi-Q states driven by higher-order interactions, Nat. Commun. **13**, 5764 (2022).

[13] O. Pietzsch, A. Kubetzka, M. Bode, and R. Wiesendanger, Observation of magnetic hysteresis at the nanometer scale by spin-polarized scanning tunneling spectroscopy, Science **292**, 2053 (2001).

[14] S. Meckler, N. Mikuszeit, A. Preßler, E. Y. Vedmedenko, O. Pietzsch, and R. Wiesendanger, Real-space observation of a right-rotating inhomogeneous cycloidal spin spiral by spin-polarized scanning tunneling microscopy in a triple axes vector magnet, Phys. Rev. Lett. **103**, 157201 (2009).

[15] M. Perini, S. Meyer, A. Kubetzka, R. Wiesendanger, S. Heinze, and K. von Bergmann, Electrical detection of domain walls and skyrmions in Co films using noncollinear magnetoresistance, Phys. Rev. Lett. **123**, 237205 (2019).

[16] S. Heinze, K. von Bergmann, M. Menzel, J. Brede, A. Kubetzka, R. Wiesendanger, G. Bihlmayer, and S. Blügel, Spontaneous atomic-scale magnetic skyrmion lattice in two dimensions, Nat. Phys. **7**, 713 (2011).

[17] N. Romming, C. Hanneken, M. Menzel, J. E. Bickel, B. Wolter, K. von Bergmann, A. Kubetzka, and R. Wiesendanger, Writing and deleting single magnetic skyrmions, Science **341**, 636 (2013).

[18] M. Hervé, B. Dupé, R. Lopes, M. Böttcher, M. D. Martins, T. Balashov, L. Gerhard, J. Sinova, and W. Wulfhekel, Stabilizing spin spirals and isolated skyrmions at low magnetic field exploiting vanishing magnetic anisotropy, Nat. Commun. **9**, 1015 (2018).

[19] S. Meyer, M. Perini, S. von Malottki, A. Kubetzka, R. Wiesendanger, K. von Bergmann, and S. Heinze, Isolated zero field sub-10 nm skyrmions in ultrathin Co films, Nat. Commun. **10**, 3823 (2019).

[20] A. Finco, P.-J. Hsu, A. Kubetzka, K. von Bergmann, and R. Wiesendanger, Tailoring noncollinear magnetism by misfit dislocation lines, Phys. Rev. B **94**, 214402 (2016).

[21] A. Finco, L. Rózsa, P.-J. Hsu, A. Kubetzka, E. Vedmedenko, K. von Bergmann, and R. Wiesendanger, Temperature-induced increase of spin spiral periods, Phys. Rev. Lett. **119**, 037202 (2017).

[22] N. Hauptmann, M. Dupé, T.-C. Hung, A. K. Lemmens, D. Wegner, B. Dupé, and A. A. Khajetoorians, Revealing the correlation between real-space structure and chiral magnetic order at the atomic scale, Phys. Rev. B **97**, 100401(R) (2018).

[23] M. Dupé, S. Heinze, J. Sinova, and B. Dupé, Stability and magnetic properties of Fe double layers on Ir(111), Phys. Rev. B **98**, 224415 (2018).

[24] P. Ferriani, S. Heinze, G. Bihlmayer, and S. Blügel, Unexpected trend of magnetic order of 3*d* transition-metal monolayers on W(001), Phys. Rev. B **72**, 024452 (2005).

[25] S. Dennler and J. Hafner, First-principles study of ultrathin magnetic Mn films on W surfaces. I. Structure and magnetism, Phys. Rev. B **72**, 214413 (2005).

[26] S. Dennler and J. Hafner, First-principles study of ultrathin magnetic Mn films on W surfaces. II. Surface diffusion, Phys. Rev. B **72**, 214414 (2005).

[27] M. Ondráček, J. Kudrnovský, I. Turek, and F. Máca, Magnetism of 3*d* transition metal atoms on W(001): Submonolayer films, J. Phys.: Conf. Ser. **61**, 894 (2007).

[28] Y. Tian and F. Jona, Nanoscale films of δ-Mn on W(001), J. Phys.: Condens. Matter **13**, 1805 (2001).

[29] M. Bode, S. Krause, L. Berbil-Bautista, S. Heinze, and R. Wiesendanger, On the preparation and electronic properties of clean W(110) surfaces, Surf. Sci. **601**, 3308 (2007).

[30] S. Loth, K. von Bergmann, M. Ternes, A. F. Otte, C. P. Lutz, and A. J. Heinrich, Controlling the state of quantum spins with electric currents, Nat. Phys. **6**, 340 (2010).

[31] I. Horcas, R. Fernández, and J. M. Gómez-Rodríguez, WSXM: A software for scanning probe microscopy and a tool for nanotechnology, Rev. Sci. Instrum. **78**, 013705 (2007).

[32] See https://www.flapw.de/MaX-6.0/.

[33] P. Kurz, F. Förster, L. Nordström, G. Bihlmayer, and S. Blügel, *Ab initio* treatment of noncollinear magnets with the full-

potential linearized augmented plane wave method, Phys. Rev. B **69**, 024415 (2004).

[34] B. Zimmermann, M. Heide, G. Bihlmayer, and S. Blügel, First-principles analysis of a homochiral cycloidal magnetic structure in a monolayer Cr on W(110), Phys. Rev. B **90**, 115427 (2014).

[35] See https://www.vasp.at/.

[36] G. Kresse and J. Furthmüller, Efficient iterative schemes for *ab initio* total-energy calculations using a plane-wave basis set, Phys. Rev. B **54**, 11169 (1996).

[37] G. Kresse and D. Joubert, From ultrasoft pseudopotentials to the projector augmented-wave method, Phys. Rev. B **59**, 1758 (1999).

[38] J. P. Perdew and Y. Wang, Accurate and simple analytic representation of the electron-gas correlation energy, Phys. Rev. B **45**, 13244 (1992).

[39] S. H. Vosko, L. Wilk, and M. Nusair, Accurate spin-dependent electron liquid correlation energies for local spin density calculations: A critical analysis, Can. J. Phys. **58**, 1200 (1980).

[40] M. Heide, G. Bihlmayer, and S. Blügel, Describing Dzyaloshinskii–Moriya spirals from first principles, Phys. B (Amsterdam) **404**, 2678 (2009).

[41] C. Li, A. J. Freeman, H. J. F. Jansen, and C. L. Fu, Magnetic anisotropy in low-dimensional ferromagnetic systems: Fe monolayers on Ag(001), Au(001), and Pd(001) substrates, Phys. Rev. B **42**, 5433 (1990).

[42] J. P. Perdew, K. Burke, and M. Ernzerhof, Generalized gradient approximation made simple, Phys. Rev. Lett. **77**, 3865 (1996).

[43] K. Tao, V. S. Stepanyuk, W. Hergert, I. Rungger, S. Sanvito, and P. Bruno, Switching a single spin on metal surfaces by a STM tip: *Ab initio* studies, Phys. Rev. Lett. **103**, 057202 (2009).

[44] P.-J. Hsu, C.-I. Lu, S.-W. Chen, W.-J. Hsueh, Y.-H. Chu, C.-H. Hsu, C. J. Butler, and M.-T. Lin, *In situ* magnetization switching of magnetic probes applied to spin-polarized scanning tunneling microscopy, Appl. Phys. Lett. **96**, 142515 (2010).

[45] R. Schmidt, C. Lazo, U. Kaiser, A. Schwarz, S. Heinze, and R. Wiesendanger, Quantitative measurement of the magnetic exchange interaction across a vacuum gap, Phys. Rev. Lett. **106**, 257202 (2011).

[46] R. Schmidt, A. Schwarz, and R. Wiesendanger, Magnetization switching utilizing the magnetic exchange interaction, Phys. Rev. B **86**, 174402 (2012).

[47] N. Hauptmann, S. Haldar, T.-C. Hung, W. Jolie, M. Gutzeit, D. Wegner, S. Heinze, and A. A. Khajetoorians, Quantifying exchange forces of a non-collinear magnetic structure on the atomic scale, Nat. Commun. **11**, 1197 (2020).

[48] D. Wortmann, S. Heinze, P. Kurz, G. Bihlmayer, and S. Blügel, Resolving complex atomic-scale spin structures by spin-polarized scanning tunneling microscopy, Phys. Rev. Lett. **86**, 4132 (2001).

[49] J. Tersoff and D. R. Hamann, Theory of the scanning tunneling microscope, Phys. Rev. B **31**, 805 (1985).

[50] S. Heinze, Simulation of spin-polarized scanning tunneling microscopy images of nanoscale non-collinear magnetic structures, Appl. Phys. A **85**, 407 (2006).

[51] B. Hardrat, A. Al-Zubi, P. Ferriani, S. Blügel, G. Bihlmayer, and S. Heinze, Complex magnetism of iron monolayers on hexagonal transition metal surfaces from first principles, Phys. Rev. B **79**, 094411 (2009).

[52] N. Romming, H. Pralow, A. Kubetzka, M. Hoffmann, S. von Malottki, S. Meyer, B. Dupé, R. Wiesendanger, K. von Bergmann, and S. Heinze, Competition of Dzyaloshinskii-Moriya and higher-order exchange interactions in Rh/Fe atomic bilayers on Ir(111), Phys. Rev. Lett. **120**, 207201 (2018).

[53] M. Hoffmann and S. Blügel, Systematic derivation of realistic spin models for beyond-Heisenberg solids, Phys. Rev. B **101**, 024418 (2020).

[54] S. Brinker, M. dos Santos Dias, and S. Lounis, The chiral biquadratic pair interaction, New J. Phys. **21**, 083015 (2019).